




Late-time draining of a thin liquid film on the outer surface of a circular cylinder

Rebecca A. McKinlay ^{*}, Alexander W. Wray [†] and Stephen K. Wilson [‡]
*Department of Mathematics and Statistics, University of Strathclyde, Livingstone Tower,
26 Richmond Street, Glasgow G1 1XH, United Kingdom*



(Received 24 November 2022; accepted 16 June 2023; published 11 August 2023)

A combination of analytical and numerical techniques is used to give a complete description of the late-time draining of a two-dimensional thin liquid film on the outer surface of a stationary horizontal circular cylinder. In this limit three regions of qualitatively different behavior emerge, namely a draining region on the upper part of the cylinder and a pendant-drop region on the lower part of the cylinder joined by a narrow inner region. In the draining region, capillarity is negligible and the film thins due to gravity. In the pendant-drop region (which, to leading order, contains all of the liquid initially on the cylinder), there is a quasistatic balance between gravity and capillarity. The matching between the draining and pendant-drop regions occurs via the inner region in which the film has a capillary-ripple structure consisting of an infinite sequence of alternating dimples and ridges. Gravity is negligible in the dimples, which are all thinner than the film in the draining region. On the other hand, gravity and capillarity are comparable in the ridges, which are all thicker than the film in the draining region. The dimples and the ridges are all asymmetric: specifically, the leading-order thickness of the dimples grows quadratically in the downstream direction but linearly in the upstream direction, whereas the leading-order film thickness in the ridges goes to zero linearly in the downstream direction but quadratically in the upstream direction. The dimples and ridges become apparent in turn as the draining proceeds, and only the first few dimples and ridges are likely to be discernible for large but finite times. However, there is likely to be a considerable period of time during which the present asymptotic solution provides a good description of the flow.

DOI: [10.1103/PhysRevFluids.8.084001](https://doi.org/10.1103/PhysRevFluids.8.084001)

I. INTRODUCTION

Liquid films coating the outer surface of a curved substrate occur in numerous industrial and biological settings and contexts, such as coating [1], painting (for example, painting of the bodies of automobiles [2]), heat transfer applications (for example, condensation onto the tubes within a heat exchanger [3]), the production of confectionery [4], the coating of orthopaedic implants [5], covering the cornea of the eye [6], and lining the lungs of land animals [7]. The special cases of

^{*}rebecca.a.mckinlay@strath.ac.uk

[†]alexander.wray@strath.ac.uk

[‡]s.k.wilson@strath.ac.uk

Published by the American Physical Society under the terms of the [Creative Commons Attribution 4.0 International](https://creativecommons.org/licenses/by/4.0/) license. Further distribution of this work must maintain attribution to the author(s) and the published article's title, journal citation, and DOI.

cylindrical and spherical substrates have received particular attention because they are of interest both in their own right and as paradigms for more complicated situations.

The pioneering work of Nusselt [8,9] considered the steady flow of a thin liquid film on the outer surface of a stationary horizontal circular cylinder fed by a prescribed flux of liquid delivered at the top of the cylinder and showed that the thickness of the film varies as $|\cos \theta|^{-1/3}$, where θ is the azimuthal angle measured anticlockwise around the cylinder from the horizontal. This analysis was later generalized to steady flow on a uniformly rotating cylinder by Duffy and Wilson [10].

Reisfeld and Bankoff [11] theoretically investigated the unsteady flow of a thin film on the outer surface of a stationary horizontal cylinder, developing a model which incorporates viscosity, gravity, capillarity, thermocapillarity, and intermolecular (van der Waals) forces, and studied both isothermal and nonisothermal situations. In particular, when the film is isothermal and van der Waals forces are negligible, they showed that the film thins on the upper part of the cylinder and that the interface develops a pendant-drop-like shape on the lower part of the cylinder. They also showed that two symmetric regions of local thinning of the film occur, and that these regions move upwards and eventually coalesce into a single region at the top of the cylinder as gravity is reduced.

Evans *et al.* [12] theoretically investigated the unsteady flow of a thin film on the outer surface of a rotating horizontal cylinder, developing a three-dimensional model which incorporates viscosity, gravity, capillarity, and centrifugation. In the special case of a two-dimensional flow on a stationary cylinder, they showed numerically that, in agreement with Reisfeld and Bankoff [11], a pendant drop forms on the lower part of the cylinder. In particular, Evans *et al.* [12] showed that this pendant drop approaches a steady state at late times, and obtained numerical solutions for its steady-state shape. They also showed that the film thickness at the top of the cylinder decreases monotonically but does not reach zero in a finite time.

Takagi and Huppert [13] theoretically and experimentally investigated the unsteady flow of a thin film with an advancing front on the outer surface of both a stationary circular cylinder and a stationary sphere. In both geometries they developed models which incorporate viscosity, gravity, and capillarity, and derived asymptotic solutions for the film thickness near the top of the substrate at late times. They found that at late times the front advances as $t^{1/2}$ for the cylinder and as $t^{1/4}$ for the sphere, and that in both cases the film near the top of the substrate thins as $t^{-1/2}$, where t denotes time.

Cachile *et al.* [14] theoretically and experimentally investigated the unsteady flow of a thin film on the outer surface of a stationary horizontal cylinder and developed a model that incorporates viscosity, gravity, and capillarity. They found that on the upper part of the cylinder there is a region in which the film thins monotonically in time as the liquid drains toward the lower part of the cylinder. They also found that a Rayleigh–Taylor-like instability occurs on the lower part of the cylinder, and determined the wavelength of the fastest-growing linear mode.

However, none of these studies obtained the complete description of the late-time behavior of the film: each focused on specific regions of the flow (such as, for example, the film thickness near the top of the cylinder or the pendant drop which forms on the lower part of the cylinder), but none of them determined how the solutions in the different regions connect together to give the complete description. A recent study which did attempt to do this, albeit for flow on a sphere rather than a cylinder, is that by Qin *et al.* [15], who theoretically investigated the unsteady flow of a thin film on the outer surface of a stationary sphere using a special case of the axisymmetric model developed by Kang *et al.* [16] that incorporates viscosity, gravity, and capillarity. They derived an asymptotic solution for the film thickness which shows that its evolution from an initially uniform film is independent of capillarity at early times. They also performed numerical simulations of the film thickness, from the results of which they inferred that four distinct “zones” of behavior emerge at late times: a “thin-film” zone on the upper part of the sphere, a quasistatic “pendant-drop” zone on the lower part of the sphere, and two narrow inner zones that connect them, namely a “dimple-ring” zone and a “ridge-ring” zone. They obtained asymptotic solutions for the film thickness in each of the zones and sought to match them to those in the neighboring zones. In particular, in the thin-film, dimple-ring, and ridge-ring zones they derived and numerically validated similarity solutions and

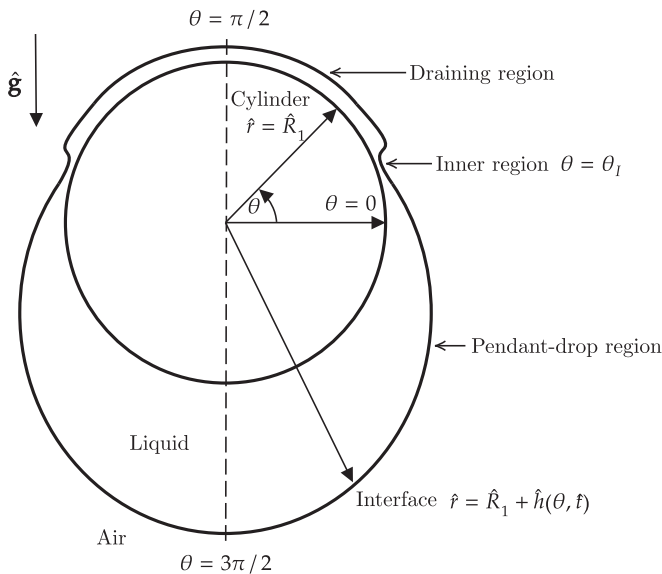


FIG. 1. The geometry of the system considered in the present work.

scaling laws for the film thickness, while in the pendant-drop zone they derived and numerically validated an analytical solution for the film thickness. We defer further discussion of this key paper to Sec. III.

In the present work we use a combination of analytical and numerical techniques to investigate the late-time draining of a two-dimensional thin film on the outer surface of a stationary horizontal circular cylinder. The two-dimensional model can, of course, be readily extended to three dimensions, and we anticipate that the corresponding analysis of this problem would have many of the same features with that described in the present work. Nevertheless, in the present work we restrict our attention to the two-dimensional problem both as an interesting problem in its own right and as an essential first step toward understanding the three-dimensional problem. Note that the two-dimensional problem can be realized physically by preventing the occurrence of a three-dimensional instability in the axial direction by, for example, using a sufficiently short cylinder and/or imposing an axial electric field (see, for example, González *et al.* [17]).

II. PROBLEM FORMULATION

We consider the unsteady two-dimensional flow of a thin film of an incompressible Newtonian liquid of constant density $\hat{\rho}$ and viscosity $\hat{\mu}$ on the outer surface of a stationary circular cylinder of radius \hat{R} with axis aligned horizontally and gravitational acceleration $\hat{\mathbf{g}}$ acting vertically downward. The geometry of the system is shown in Fig. 1. Figure 1 also shows the three regions of qualitatively different behavior which emerge at late times: these regions will be analyzed in detail in Secs. IV, V, and VI, respectively. The liquid film is surrounded by air at constant atmospheric pressure \hat{p}_a , and the liquid-gas interface has constant coefficient of surface tension $\hat{\sigma}$. We use two-dimensional polar coordinates (\hat{r}, θ) centered on the axis of the cylinder, with θ measured anticlockwise from the horizontal on the right-hand side of the cylinder. Throughout the present work we assume that the flow has left-to-right symmetry, and so we restrict our attention to the left-hand side of the cylinder and hence work in the domain $\pi/2 \leq \theta \leq 3\pi/2$. The thickness of the film at time \hat{t} is denoted by $\hat{h}(\theta, \hat{t})$, so that the interface of the liquid is located at $\hat{r} = \hat{R} + \hat{h}(\theta, \hat{t})$. The film has a uniform initial thickness $\hat{h}|_{\hat{t}=0} = \hat{h}_0$. The liquid has pressure $\hat{p}(\hat{r}, \theta)$ and velocity $\hat{u}(\hat{r}, \theta)\mathbf{e}_r + v(\hat{r}, \theta)\mathbf{e}_\theta$, where \mathbf{e}_r and \mathbf{e}_θ denote the unit vectors in the radial and azimuthal directions, respectively. We

nondimensionalize and scale the system according to

$$\hat{r} = \hat{R}(1 + \epsilon R), \quad \hat{h} = \epsilon \hat{R}H, \quad \hat{p} - \hat{p}_a = \frac{\hat{\mu} \hat{U}_{\text{ref}}}{\hat{R}} P, \quad \hat{u} = \epsilon^3 \hat{U}_{\text{ref}} U, \quad \hat{v} = \epsilon^2 \hat{U}_{\text{ref}} V, \quad \hat{t} = \frac{\hat{R}}{\epsilon^2 \hat{U}_{\text{ref}}} T, \quad (1)$$

where $\hat{U}_{\text{ref}} = \hat{\rho} \hat{g} \hat{R}^2 / \hat{\mu}$ is a characteristic velocity scale, to find that at leading order in the limit of small aspect ratio $\epsilon = \hat{h}_0 / \hat{R} \rightarrow 0$ the system is governed by the lubrication equations, namely

$$U_R + V_\theta = 0, \quad P_R = 0, \quad V_{RR} = P_\theta + \cos \theta, \quad (2)$$

subject to the normal and tangential stress conditions at the interface,

$$P|_{R=H} = \frac{1}{\epsilon \gamma} [1 - \epsilon(H + H_{\theta\theta})], \quad V_R|_{R=H} = 0, \quad (3)$$

where $\gamma = \hat{\mu} \hat{U}_{\text{ref}} / (\epsilon \hat{\sigma}) = \hat{\rho} \hat{g} \hat{R}^2 / (\epsilon \hat{\sigma})$ is an appropriately defined capillary number of order unity (see, for example, Oron *et al.* [18] and Craster and Matar [19]). These can be solved in the usual way to determine the pressure P and the azimuthal velocity V , and hence the kinematic condition yields the governing thin-film equation

$$H_T + Q_\theta = 0, \quad (4)$$

where $Q = Q(\theta, T)$ defined by

$$Q = \int_0^H V(R, \theta) dR = -\frac{1}{3} H^3 \cos \theta + \frac{1}{3\gamma} H^3 (H + H_{\theta\theta})_\theta \quad (5)$$

is the azimuthal volume flux per unit width, subject to the initial condition

$$H|_{T=0} = 1. \quad (6)$$

While this equation would normally be solved subject to periodic conditions, we instead exploit the symmetry of the system to impose the symmetry conditions

$$H_\theta = H_{\theta\theta\theta} = 0 \quad \text{at} \quad \theta = \frac{\pi}{2} \quad \text{and} \quad \frac{3\pi}{2}. \quad (7)$$

Equation (4) with Q given by Eq. (5) and subject to Eqs. (6) and (7) is the basis of all of the analysis that follows.

Numerical solutions of Eq. (4) are obtained using a fully implicit centered-finite-difference code that is second order in both space and time. This code has previously been successfully used to solve other problems (see, for example, Wray *et al.* [20] and Wray and Cimpeanu [21]). To enable computations to be performed up to the longest final times of up to $T = O(10^{11})$ required to validate the present asymptotic solution while still resolving the fine spatial structures that occur, we used a nonuniform grid formulation. The grid spacing is reduced smoothly from 5×10^{-3} in the bulk of the domain to 10^{-6} within $\pi/18$ of the azimuthal location of the inner region, denoted by $\theta = \theta_1$ ($\pi/2 \leq \theta_1 \leq 3\pi/2$). The inner region is shown in Fig. 1 and analyzed in Sec. VI. Derivatives are computed using standard centered finite differences, with convergence being verified in both space and time. The linear algebra required to compute the Newton–Raphson iterations for the fully implicit time-stepping was performed using the Eigen C++ template library for linear algebra [22].

In the present work we investigate the draining of the film at late times. However, for completeness, we also give a brief account of the draining of the initially uniform film at early times in the Appendix.

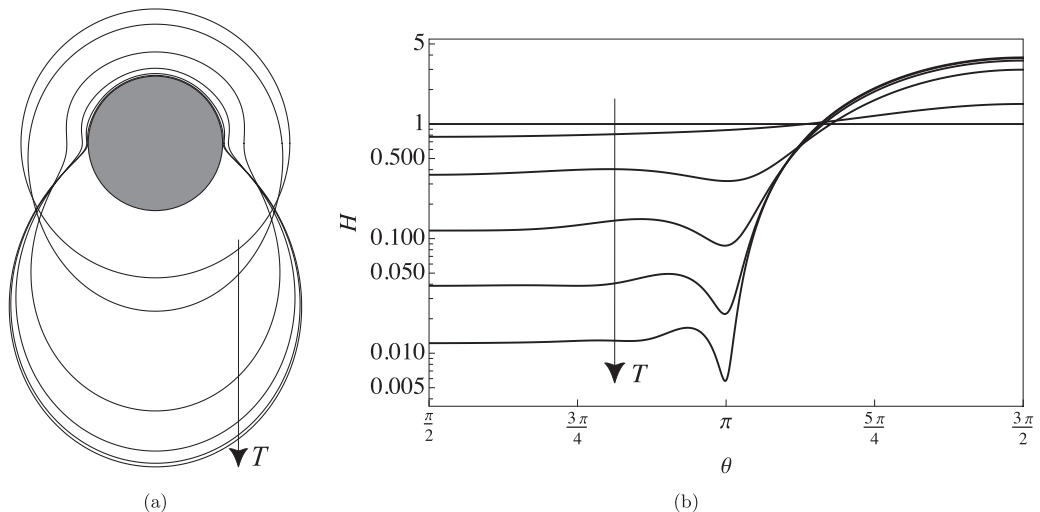


FIG. 2. Snapshots of the interface for $\gamma = \gamma_\pi$ given by Eq. (8) at times $T = 0, 10^0, 10^1, 10^2, 10^3$, and 10^4 . The arrows indicate the direction of increasing time. (a) Polar plot in which the film thickness has been exaggerated for illustrative purposes by using the artificial value $\epsilon = 1$. (b) Semi-log plot showing the film thickness H as a function of θ .

III. LATE-TIME DRAINING

As mentioned in Sec. I, and as sketched in Fig. 1, three regions of qualitatively different behavior emerge at late times. As in the corresponding problem of flow on a spherical substrate studied by Qin *et al.* [15], different balances of forces determine the dominant behavior in each region, leading to different simplifications of the governing equation (4). Therefore, the overall evolution of the film at late times can be investigated by analyzing each region separately and performing the appropriate asymptotic matching between them. On the upper part of the cylinder, gravity dominates capillarity, resulting in a draining flow which causes the film to thin, corresponding to the thin-film zone of Qin *et al.* [15] in the spherical case. We shall refer to this region as the “draining region” and it will be discussed in Sec. IV. On the other hand, on the lower part of the cylinder, gravity and capillarity balance, resulting in the formation of a quasistatic pendant drop, corresponding to the pendant-drop zone of Qin *et al.* [15] in the spherical case. We shall refer to this region as the “pendant-drop region” and it will be discussed in Sec. V.

The draining and pendant-drop regions do not match directly with each other, but do so via a narrow intermediate region. We shall refer to this region as the “inner region.” We will show that this inner region consists of an infinite sequence of alternating “dimples” (i.e., narrow regions in which the film thickness has a local minimum) and “ridges” (i.e., narrow regions in which the film thickness has a local maximum). The inner region and, in particular, the qualitative difference between the structure of the inner region and that described by Qin *et al.* [15] in the spherical case will be discussed in Sec. VI.

Figure 2 shows snapshots of the interface for

$$\gamma = \gamma_\pi = \frac{8\pi}{\pi^2 - 8} \simeq 13.4428 \quad (8)$$

at various times. In Sec. V it will be shown that this value of γ leads to $\theta_1 = \pi$ (i.e., the inner region is located at the waist of the cylinder), and this is confirmed by the results shown in Fig. 2. Figure 3 shows snapshots of the interface for various values of γ at time $T = 10^4$. In particular, Fig. 3 shows that the effect of varying γ is mainly to change the location of the inner region θ_1 and,

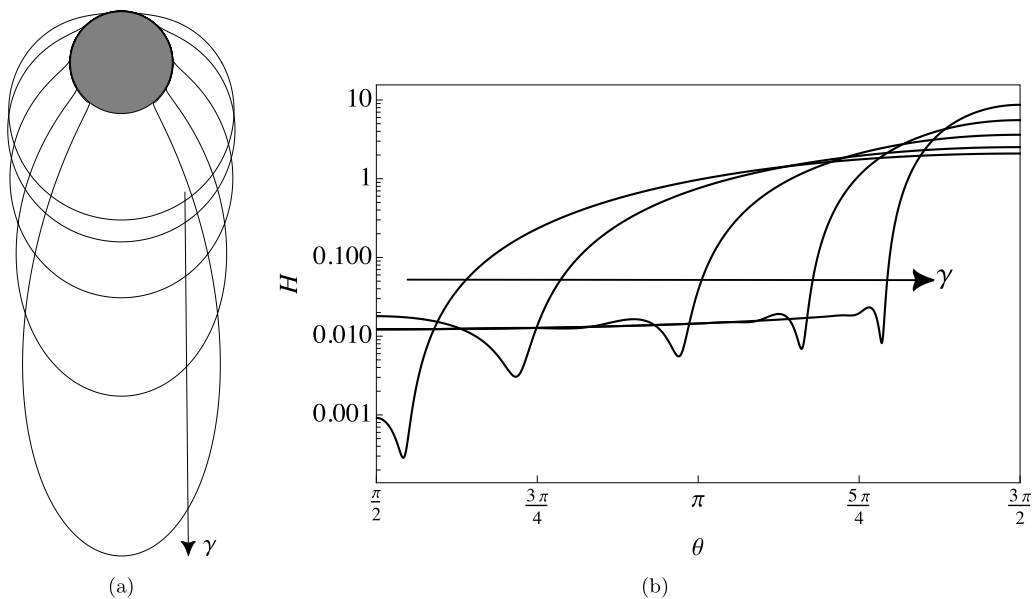


FIG. 3. Snapshots of the interface for $\gamma = 10^{-1}, 10^0, 10^1, 10^2$, and 10^3 at time $T = 10^4$. The arrows indicate the direction of increasing γ . (a) Polar plot in which the film thickness has been exaggerated for illustrative purposes by using the artificial value $\epsilon = 1$. (b) Semi-log plot showing the film thickness H as a function of θ .

correspondingly, the widths of the draining and pendant-drop regions. Specifically, decreasing the value of γ , corresponding to weakening gravity, results in a narrower draining region and a wider pendant-drop region, consistent with the numerical results of Reisfeld and Bankoff [11] mentioned in Sec. I. Figure 4 shows the film thickness H for $\gamma = \gamma_\pi$ given by Eq. (8) at time $T = 10^{10}$. In particular, while only the first dimple and ridge are immediately apparent in Figs. 2, 3, and 4(a), the second and third dimple and ridge are discernible in the enlargement of Fig. 4(a) near $\theta = \theta_1 = \pi$ shown in Fig. 4(b).

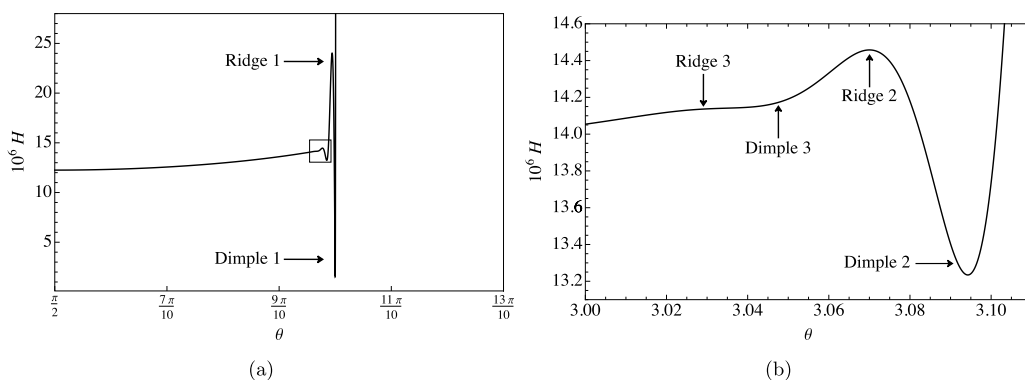


FIG. 4. The film thickness H for $\gamma = \gamma_\pi$ given by Eq. (8) at time $T = 10^{10}$. (a) Solution for $\pi/2 \leq \theta \leq 13\pi/10$. The rectangle indicates the location of the enlargement shown in panel (b). (b) Enlargement of panel (a) near $\theta = \theta_1 = \pi$.

IV. DRAINING REGION

The results of the present numerical calculations indicate that at late times the film becomes thin in the draining region. Therefore, we seek a late-time asymptotic solution in which $H \ll 1$, and hence at leading order the governing equation (4) becomes simply

$$H_T + \left(-\frac{1}{3}H^3 \cos \theta\right)_\theta = 0. \quad (9)$$

We seek a separable solution to Eq. (9) of the form $H(\theta, T) = \eta(\theta)T^n$, yielding

$$nT^{n-1}\eta + \left(-\frac{1}{3}T^{3n}\eta^3 \cos \theta\right)_\theta = 0. \quad (10)$$

Balancing powers of n in Eq. (10) yields $n = -1/2$, and hence Eq. (9) has a solution of the form

$$H(\theta, T) = \eta(\theta)T^{-1/2}, \quad (11)$$

where the function $\eta = \eta(\theta)$ satisfies the first-order ordinary differential equation (ODE)

$$\frac{d}{d\theta}(\eta^3 \cos \theta) + \frac{3}{2}\eta = 0. \quad (12)$$

Solving Eq. (12) subject to the symmetry conditions (7) yields

$$\eta(\theta) = \begin{cases} \left(\frac{3}{2}\varphi(\theta)\right)^{1/2} & \text{for } \frac{\pi}{2} \leq \theta \leq \pi, \\ \left(\frac{\sqrt{\pi} \Gamma(\frac{1}{3})}{|\cos \theta|^{2/3} \Gamma(\frac{5}{6})} - \frac{3}{2}\varphi(\theta)\right)^{1/2} & \text{for } \pi \leq \theta \leq \frac{3\pi}{2}, \end{cases} \quad (13)$$

where $\varphi(\theta)$ is the hypergeometric function

$$\varphi(\theta) = {}_2F_1\left(\frac{1}{3}, \frac{1}{2}; \frac{4}{3}; (\cos \theta)^2\right). \quad (14)$$

Equation (11) shows that the film in the draining region thins as $T^{-1/2}$, consistent with the result of Takagi and Huppert [13] for a film with an advancing front mentioned in Sec. I, and that H is a monotonically increasing function of θ . In particular, this means that at any instant in time the leading-order film thickness in this region increases from a minimum value of

$$H\left(\frac{\pi}{2}, T\right) = \sqrt{\frac{3}{2}}T^{-1/2} \quad (15)$$

at the top of the cylinder (i.e., at $\theta = \pi/2$) to a maximum value at $\theta = \theta_1$.

Substituting the solution for H in the draining region (11) into the flux (5) shows that the contributions to the flux due to gravity and capillarity are

$$Q_{\text{grav}} = -\frac{1}{3}H^3 \cos \theta = O(T^{-3/2}) \ll 1, \quad (16)$$

$$Q_{\text{cap}} = \frac{1}{3\gamma}H^3(H + H_{\theta\theta})_\theta = O(T^{-2}) \ll 1, \quad (17)$$

respectively. In particular, Eqs. (16) and (17) show that $Q_{\text{cap}} \ll Q_{\text{grav}} \ll 1$ at late times, confirming the validity of neglecting capillarity in the draining region.

Figure 5 shows a log-log plot of H , Q_{grav} , and Q evaluated at the top of the cylinder obtained from numerical solutions of Eq. (4) for $\gamma = \gamma_\pi$ given by Eq. (8) as functions of T , and compares them with the corresponding late-time asymptotic scalings $T^{-1/2}$, $T^{-3/2}$, and $T^{-3/2}$ obtained from Eqs. (11) and (16). In particular, Fig. 5 confirms that the interface has the predicted asymptotic behavior at sufficiently late times. This conclusion is confirmed by the numerical values shown in

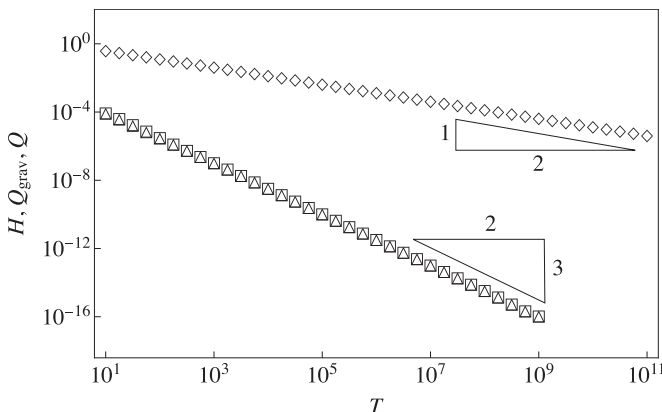


FIG. 5. Log-log plot of H (diamonds), Q_{grav} (triangles), and Q (squares) evaluated at the top of the cylinder for $\gamma = \gamma_\pi$ given by Eq. (8) as functions of T , and the corresponding late-time asymptotic scalings $T^{-1/2}$, $T^{-3/2}$, and $T^{-3/2}$. Note that the triangles and the squares almost lie on top of each other.

Table I, which shows that the asymptotic scalings are in excellent agreement with the slopes of the corresponding lines of best fit to the numerical results for $T \geq 10^{9/4}$ shown in Fig. 5. Note that, as a consequence of the symmetry conditions (7), $Q_{\text{cap}} \equiv 0$ at the top of the cylinder, and so is omitted from both Fig. 5 and Table I.

Figure 6 shows snapshots of the scaled film thickness $\eta = HT^{1/2}$ for $\gamma = \gamma_\pi$ given by Eq. (8) at various times together with the leading-order asymptotic solution in the draining region (11), confirming that the interface does indeed approach the asymptotic solution at late times.

To perform the asymptotic matching with the inner region, it will be useful to determine the azimuthal volume flux out of the draining region, denoted by $Q_{\text{drain}} = Q(\theta_1, T) = Q_{\text{drain}}(T)$. Integrating the governing equation (4) across the draining region gives an expression for Q_{drain} , namely

$$Q_{\text{drain}} = - \int_{\pi/2}^{\theta_1} H_T d\theta, \quad (18)$$

where H is given by Eq. (11), and hence

$$Q_{\text{drain}} = \frac{1}{2} T^{-3/2} \int_{\pi/2}^{\theta_1} \eta(\theta) d\theta, \quad (19)$$

showing that the flux out of the draining region decreases as $T^{-3/2}$ at late times.

TABLE I. The late-time asymptotic scalings for H , Q_{grav} , and Q evaluated at the top of the cylinder, and the slopes of the corresponding lines of best fit to the numerical results for $T \geq 10^{9/4}$ shown in Fig. 5.

	Asymptotic scaling	Numerical result
H	-0.5	-0.5021
Q_{grav}	-1.5	-1.5045
Q	-1.5	-1.4999

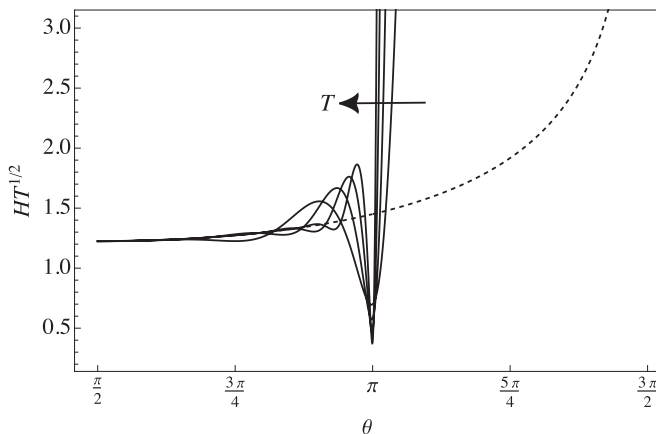


FIG. 6. Snapshots of the scaled film thickness $\eta = HT^{1/2}$ for $\gamma = \gamma_\pi$ given by Eq. (8) at times $T = 10^3$, 10^4 , 10^5 , and 10^6 . The arrow indicates the direction of increasing time. The dashed line shows the leading-order asymptotic solution in the draining region (11).

V. PENDANT-DROP REGION

The results of the present numerical calculations indicate that at late times the pendant-drop region shown in Figs. 2(a) and 3(a) is quasistatic so that $H = H(\theta)$ is independent of T , and hence at leading order the governing equation (4) becomes

$$(H + H_{\theta\theta})_\theta = \gamma \cos \theta. \quad (20)$$

Equation (20) is a third-order ODE for the film thickness H which requires three boundary conditions. At the edge of the pendant-drop region, the interface approaches the surface of the cylinder tangentially, i.e., H satisfies the two boundary conditions

$$H|_{\theta=\theta_1} = 0, \quad (21)$$

$$H_\theta|_{\theta=\theta_1} = 0. \quad (22)$$

The third boundary condition is the symmetry condition at the bottom of the cylinder (7).

Solving Eq. (20) subject to Eqs. (21), (22), and (7) yields the solution for H in the pendant-drop region, namely

$$H = \frac{\gamma}{4} [(3\pi - 2\theta) \cos \theta - (3\pi - 2\theta_1) \cos \theta_1 + \{2 + (3\pi - 2\theta_1) \tan \theta_1\} (\sin \theta - \sin \theta_1)] \quad (23)$$

for $\theta_1 \leq \theta \leq 3\pi/2$.

The solution (23) contains an unknown constant, namely the azimuthal location of the inner region θ_1 , which can be determined by imposing global conservation of mass. To leading order, all of the liquid initially on the cylinder is contained within the pendant-drop region, so that

$$\int_{\theta_1}^{3\pi/2} H d\theta = \int_{\pi/2}^{3\pi/2} H(0) d\theta = \pi. \quad (24)$$

Substituting the asymptotic solution for H given by Eq. (23) into the global mass conservation condition (24) and evaluating the integral yields an implicit equation for θ_1 in terms of γ , namely

$$\gamma = \frac{8\pi \cos \theta_1}{4[1 + \cos(2\theta_1)] - (3\pi - 2\theta_1)[3\pi - 2\theta_1 + \sin(2\theta_1)]}. \quad (25)$$

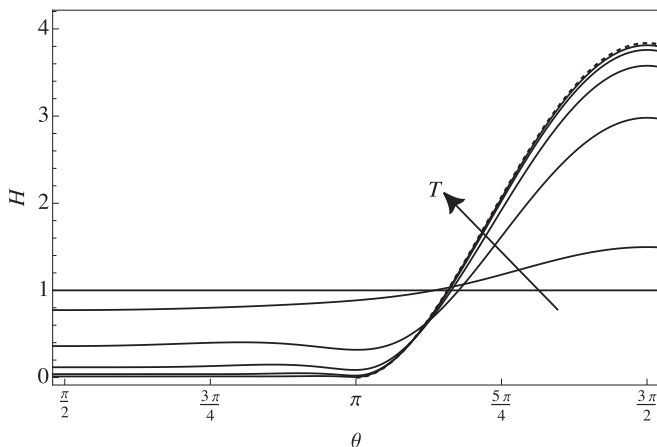


FIG. 7. Snapshots of the film thickness H for $\gamma = \gamma_\pi$ given by Eq. (8) at times $T = 0, 10^0, 10^1, 10^2, 10^3,$ and 10^4 . The arrow indicates the direction of increasing time. The (barely visible) dashed line shows the leading-order asymptotic solution in the pendant-drop region (23).

Note that, unlike the corresponding equation in the spherical case obtained by Qin *et al.* [15], it is not possible to invert Eq. (25) to obtain an explicit expression for θ_1 in terms of γ . In particular, as mentioned in Sec. III, Eq. (25) predicts that $\theta_1 = \pi$ (i.e., the inner region is located at the waist of the cylinder) when $\gamma = \gamma_\pi$ given by Eq. (8).

Figure 7 shows snapshots of the film thickness H for $\gamma = \gamma_\pi$ given by Eq. (8) at various times together with the leading-order asymptotic solution in the pendant-drop region (23), confirming that the interface does indeed approach the asymptotic solution at late times. In particular, Fig. 7 shows that the leading-order film thickness in this region increases from zero at $\theta_1 = \pi$ to a maximum value of

$$H\left(\frac{3\pi}{2}\right) = -\frac{\gamma}{4}\{(3\pi - 2\theta_1)\cos\theta_1 + [2 + (3\pi - 2\theta_1)\tan\theta_1](1 + \sin\theta_1)\} = \frac{2\pi(\pi - 2)}{\pi^2 - 8} \simeq 3.8366 \quad (26)$$

at the bottom on the cylinder.

Figure 8 shows the relationship between γ and θ_1 . Specifically, Fig. 8 shows that the asymptotic expression (25) is in very good agreement with the position of the inner region calculated from numerical solutions of the governing equation (4) for five values of γ at time $T = 10^4$. In particular, Fig. 8 shows that θ_1 is a monotonically increasing function of γ , confirming that weakening gravity results in a narrower draining region and a wider pendant-drop region, consistent with the results shown in Fig. 3.

Substituting Eq. (25) into Eq. (23) and taking the limit $\theta \rightarrow \theta_1^+$ yields the local behavior of the interface in the pendant-drop region as it approaches the inner region, namely

$$H = \frac{\pi[\sin(2\theta_1) - (3\pi - 2\theta_1)]}{4[1 + \cos(2\theta_1)] - (3\pi - 2\theta_1)[3\pi - 2\theta_1 + \sin(2\theta_1)]}(\theta - \theta_1)^2 + O[(\theta - \theta_1)^3] \quad \text{as } \theta \rightarrow \theta_1^+. \quad (27)$$

This result will be used in Sec. VIA when performing the asymptotic matching of the solution in the pendant-drop region to that in dimple 1.

VI. INNER REGION

The matching between the draining and pendant-drop regions occurs via the inner region located at $\theta = \theta_1$. Figure 9 shows a sketch of the asymptotic structure of the inner region, which, as

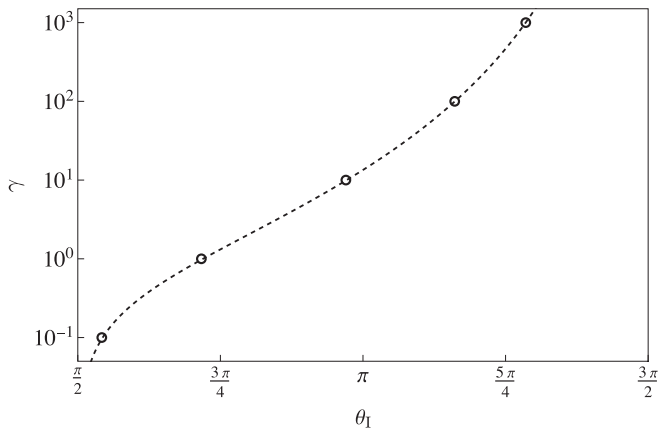


FIG. 8. The relationship between γ and θ_1 . The dashed line shows the asymptotic expression (25), and the circles show the position of the inner region calculated from numerical solutions of the governing equation (4) for $\gamma = 10^{-1}, 10^0, 10^1, 10^2,$ and 10^3 at $T = 10^4$.

mentioned above, consists of an infinite sequence of alternating dimples and ridges. This “capillary-ripple” structure is qualitatively different from that of one dimple-ring zone and one ridge-ring zone described by Qin *et al.* [15] in the spherical case. In fact, we anticipate that a corresponding infinite sequence of alternating dimple-ring zones and ridge-ring zones also occurs in the spherical case. The flaw in the analysis of Qin *et al.* [15] is that the flux out of their thin-film zone is not, in fact, of the same order as the fluxes due to gravity and capillarity in their ridge-ring zone. This mismatch is not apparent in their numerical results because they never computed beyond a final time of $T = O(10^5)$ (compared to a final time of $T = O(10^{11})$ used in the present work), and (extrapolating from the behavior of the present solution described in Sec. VIC), the other dimple-ring and ridge-ring zones presumably only become apparent at larger values of T . However, capillary-ripple structures similar to that described here have been found in other situations, most famously by Wilson and Jones [23], who showed that an infinite sequence of steady dimples and ridges is necessary to match a thin liquid film of uniform thickness flowing down a vertical wall to a quiescent pool of liquid. Following this pioneering work, similar structures have been found in rimming flow [24], levitated drops [25], liquid films or drops on inclined planes [26–28], elastic-plated gravity currents [29], and Leidenfrost levitation of particles [30].

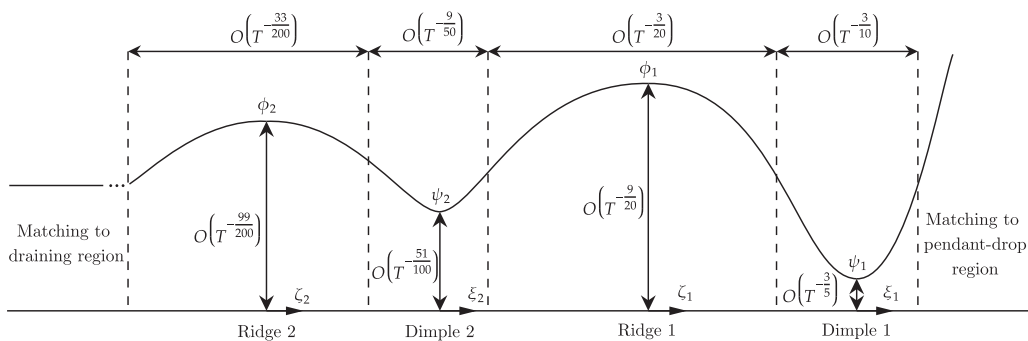


FIG. 9. A sketch of the asymptotic structure of the inner region.

We determine the asymptotic solutions for H in dimple 1 and ridge 1 in Secs. [VIA](#) and [VIB](#), respectively. We then generalize this analysis to determine the asymptotic solutions for H in dimple n and ridge n for $n = 2, 3, 4, \dots$ in Sec. [VIC](#).

A. Dimple 1

The results of the present numerical calculations indicate that, as Fig. 4 illustrates, dimple 1 is narrow and thin (specifically, thinner than the draining region). Motivated by these numerical results, we seek a leading-order asymptotic solution for H in the self-similar form

$$H = \frac{\psi_1(\xi_1)}{T^{\alpha_1}}, \quad \theta - \theta_1 = \frac{\xi_1}{T^{\beta_1}}, \quad (28)$$

where the exponents $\alpha_1 > 1/2$ and $\beta_1 > 0$ are positive constants which we shall determine.

Equating the flux out of the draining region given by Eq. (19) with the flux in dimple 1 obtained from Eq. (5) with Eq. (28) yields

$$T^{-3/2}K = -\frac{1}{3}\psi_1^3 T^{-3\alpha_1} \cos \theta_1 + \frac{1}{3\gamma}\psi_1^3 [T^{-4\alpha_1+\beta_1}\psi_{1\xi_1} + T^{-4\alpha_1+3\beta_1}\psi_{1\xi_1\xi_1\xi_1}], \quad (29)$$

where

$$K = \frac{3\gamma}{2} \int_{\pi/2}^{\theta_1} \eta(\theta) d\theta > 0 \quad (30)$$

is a positive constant.

Considering the possible leading-order balances in Eq. (29) and imposing asymptotic matching with the pendant-drop region yields two equations relating α_1 and β_1 , namely

$$-\frac{3}{2} = -4\alpha_1 + 3\beta_1 \quad \text{and} \quad -\alpha_1 + 2\beta_1 = 0, \quad (31)$$

and so α_1 and β_1 are given by

$$\alpha_1 = \frac{3}{5}, \quad \beta_1 = \frac{3}{10}, \quad (32)$$

and hence the solution for H given by Eq. (28) becomes

$$H = \frac{\psi_1(\xi_1)}{T^{3/5}}, \quad \theta - \theta_1 = \frac{\xi_1}{T^{3/10}}, \quad (33)$$

where the function $\psi_1 = \psi_1(\xi_1)$ satisfies

$$\psi_1^3 \psi_{1\xi_1\xi_1\xi_1} = K. \quad (34)$$

In particular, Eq. (33) shows that dimple 1 has the same asymptotic scalings as the dimple-ring zone in the spherical case found by Qin *et al.* [15]. Note that equation (34) (sometimes referred to as ‘‘the current equation’’) arises in a variety of other draining and coating flows (see, for example, Lamstaes and Eggers [31] and van Limbeek *et al.* [32]).

Substituting the solution for H given by Eq. (33) into the flux (5) shows that

$$Q_{\text{grav}} = -\frac{1}{3}H^3 \cos \theta = O(T^{-9/5}) \ll 1, \quad (35)$$

$$Q_{\text{cap}} = \frac{1}{3\gamma}H^3(H + H_{\theta\theta})_{\theta} = O(T^{-3/2}) \ll 1, \quad (36)$$

confirming the validity of neglecting gravity in dimple 1.

Figure 10 shows a log–log plot of H , Q_{grav} , Q_{cap} , and Q evaluated at the minimum of dimple 1 obtained from numerical solutions of Eq. (4) for $\gamma = \gamma_{\pi}$ given by Eq. (8) as function of T , and compares them with the corresponding late-time asymptotic scalings $T^{-3/5}$, $T^{-9/5}$, $T^{-3/2}$, and $T^{-3/2}$ obtained from Eqs. (33), (35), and (36). In particular, Fig. 10 and Table II confirm that the interface has the predicted asymptotic behavior at sufficiently late times.

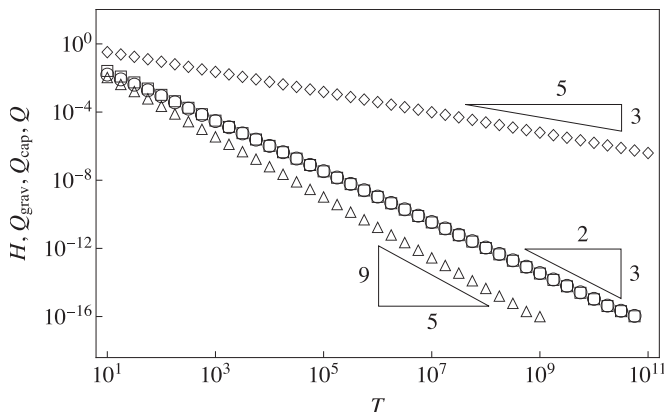


FIG. 10. Log–log plot of H (diamonds), Q_{grav} (triangles), Q_{cap} (circles), and Q (squares) evaluated at the minimum of dimple 1 for $\gamma = \gamma_\pi$ given by Eq. (8) as functions of T , and the corresponding late-time asymptotic scalings $T^{-3/5}$, $T^{-9/5}$, $T^{-3/2}$, and $T^{-3/2}$. Note that the circles and the squares almost lie on top of each other.

The shape of the interface of dimple 1 is determined by solving Eq. (34) for ψ_1 subject to appropriate far-field and boundary conditions. The first condition arises from matching with the pendant-drop region, i.e.,

$$\psi_{1\xi_1\xi_1} |_{\xi_1 \rightarrow +\infty} = H_{\theta\theta} |_{\theta \rightarrow \theta_1^+} = L_0 := \frac{2\pi[\sin(2\theta_1) - (3\pi - 2\theta_1)]}{4[1 + \cos(2\theta_1)] - (3\pi - 2\theta_1)[3\pi - 2\theta_1 + \sin(2\theta_1)]}, \quad (37)$$

where H is given by Eq. (27). The second condition arises from matching with ridge 1, i.e.,

$$\psi_{1\xi_1\xi_1} |_{\xi_1 \rightarrow -\infty} = 0. \quad (38)$$

Note that Eqs. (37) and (38) mean that the leading-order film thickness in ridge 1 grows quadratically in the limit $\xi_1 \rightarrow +\infty$ but only linearly in the limit $\xi_1 \rightarrow -\infty$. The third condition fixes the location of the minimum of ψ_1 at $\xi_1 = 0$, i.e.,

$$\psi_{1\xi_1} |_{\xi_1=0} = 0. \quad (39)$$

The constants K and L_0 can be scaled out of the problem (34) and (37)–(39) by setting

$$\psi_1 = K^{2/5} L_0^{-3/5} \tilde{\psi}, \quad \xi_1 = K^{1/5} L_0^{-4/5} \tilde{\xi}, \quad (40)$$

yielding the rescaled (parameter-free) problem

$$\tilde{\psi}^3 \tilde{\psi}_{\tilde{\xi}\tilde{\xi}\tilde{\xi}} = 1, \quad (41)$$

$$\tilde{\psi}_{\tilde{\xi}\tilde{\xi}} |_{\tilde{\xi} \rightarrow +\infty} = 1, \quad (42)$$

TABLE II. The late-time asymptotic scalings for H , Q_{grav} , Q_{cap} , and Q in dimple 1, and the slopes of the lines of best fit to the numerical results for $T \geq 10^{9/4}$ shown in Fig. 10.

	Asymptotic scaling	Numerical result
H	-0.6	-0.5974
Q_{grav}	-1.8	-1.7773
Q_{cap}	-1.5	-1.4877
Q	-1.5	-1.4953

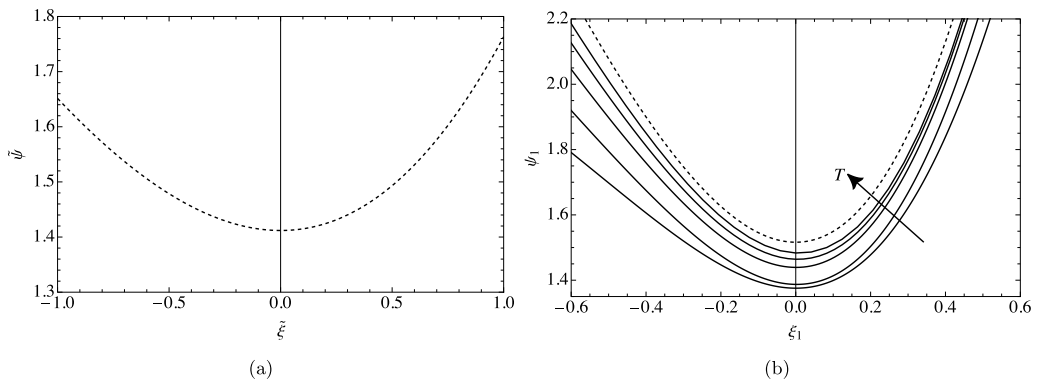


FIG. 11. (a) Solution of the rescaled problem (41)–(44) expressed in rescaled variables $\tilde{\xi}$ and $\tilde{\psi}$. (b) Snapshots of the film thickness for $\gamma = \gamma_\pi$ given by Eq. (8) at times $T = 10^2, 10^3, 10^4, 10^5,$ and 10^6 expressed in scaled variables ξ_1 and ψ_1 . The arrow indicates the direction of increasing time. The dashed line shows the leading-order asymptotic solution in dimple 1 (33).

$$\tilde{\psi}_{\tilde{\xi}\tilde{\xi}}|_{\tilde{\xi} \rightarrow -\infty} = 0, \quad (43)$$

$$\tilde{\psi}_{\tilde{\xi}}|_{\tilde{\xi}=0} = 0. \quad (44)$$

Figure 11(a) shows the numerical solution of the rescaled problem (41)–(44) expressed in rescaled variables $\tilde{\xi}$ and $\tilde{\psi}$, and Fig. 11(b) shows snapshots of the film thickness for $\gamma = \gamma_\pi$ given by Eq. (8) at various times together with the leading-order asymptotic solution in dimple 1 (33) expressed in scaled variables ξ_1 and ψ_1 , confirming that the interface does indeed approach the asymptotic solution at late times. In particular, the limiting value of the slope of the interface in the rescaled problem as $\tilde{\xi} \rightarrow -\infty$ is found to be

$$\tilde{\psi}|_{\tilde{\xi} \rightarrow -\infty} = -\tilde{m}, \quad (45)$$

where

$$\tilde{m} = 0.9626. \quad (46)$$

This result will be used in Sec. VIB when performing the asymptotic matching between dimple 1 and ridge 1, and again in Sec. VIC when performing the asymptotic matching between dimple n and ridge n .

B. Ridge 1

The results of the present numerical calculations indicate that, as Fig. 4 also illustrates, ridge 1 is narrow (but wider than dimple 1) and thin (but thicker than the draining region). Motivated by these numerical results, we seek a leading-order asymptotic solution for H in the self-similar form

$$H = \frac{\phi_1(\zeta_1)}{T^{\delta_1}}, \quad \theta - \theta_1 = \frac{\zeta_1}{T^{\lambda_1}}, \quad (47)$$

where the exponents $0 < \delta_1 < 1/2$ and $0 < \lambda_1 < \beta_1$ are positive constants which we shall determine.

Equating the flux out of the draining region given by Eq. (19) with the flux in ridge 1 obtained from Eq. (5) with Eq. (47) yields

$$T^{-3/2}K = -\frac{1}{3}\phi_1^3 T^{-3\delta_1} \cos \theta_1 + \frac{1}{3\gamma}\phi_1^3 [T^{-4\delta_1+\lambda_1} \phi_{1\zeta_1} + T^{-4\delta_1+3\lambda_1} \phi_{1\zeta_1\zeta_1}], \quad (48)$$

where the constant K is again given by Eq. (30).

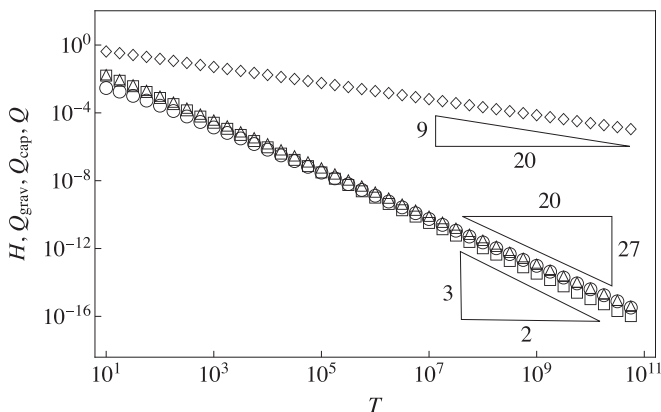


FIG. 12. Log-log plot of H (diamonds), Q_{grav} (triangles), Q_{cap} (circles), and Q (squares) evaluated at the maximum of ridge 1 for $\gamma = \gamma_\pi$ given by Eq. (8) as functions of T , and the corresponding late-time asymptotic scalings $T^{-9/20}$, $T^{-27/20}$, $T^{-27/20}$, and $T^{-3/2}$. Note that the triangles, circles, and squares almost lie on top of each other.

Analogously to the corresponding analysis of dimple 1 described in Sec. VI A, considering the possible leading-order balances in Eq. (48) and imposing asymptotic matching with dimple 1 yields two equations relating δ_1 and λ_1 , namely

$$\delta_1 - 3\lambda_1 = 0 \quad \text{and} \quad -\delta_1 + \lambda_1 = -\frac{3}{10}, \quad (49)$$

and so δ_1 and λ_1 are given by

$$\delta_1 = \frac{9}{20}, \quad \lambda_1 = \frac{3}{20}, \quad (50)$$

and hence the solution for H given by Eq. (47) becomes

$$H = \frac{\phi_1(\zeta_1)}{T^{9/20}}, \quad \theta - \theta_1 = \frac{\zeta_1}{T^{3/20}}, \quad (51)$$

where the function $\phi_1 = \phi_1(\zeta_1)$ satisfies

$$\phi_{1\zeta_1\zeta_1} = \gamma \cos \theta_1. \quad (52)$$

In particular, Eq. (51) shows that ridge 1 has the same asymptotic scalings as the ridge-ring zone in the spherical case found by Qin *et al.* [15].

Substituting the solution for H given by Eq. (51) into the flux (5) shows that

$$Q_{\text{grav}} = -\frac{1}{3}H^3 \cos \theta = O(T^{-27/20}) \ll 1, \quad (53)$$

$$Q_{\text{cap}} = \frac{1}{3\gamma}H^3(H + H_{\theta\theta})_\theta = O(T^{-27/20}) \ll 1, \quad (54)$$

confirming that gravity and capillarity are comparable in ridge 1.

Figure 12 shows a log-log plot of H , Q_{grav} , Q_{cap} , and Q evaluated at the maximum of ridge 1 obtained from numerical solutions of Eq. (4) for $\gamma = \gamma_\pi$ given by Eq. (8) as a function of T , and compares them with the corresponding late-time asymptotic scalings $T^{-9/20}$, $T^{-27/20}$, $T^{-27/20}$, and $T^{-3/2}$ obtained from Eqs. (51), (53), and (54). In particular, Fig. 12 and Table III confirm that the interface has the predicted asymptotic behavior at sufficiently late times.

TABLE III. Late-time asymptotic scalings for H , Q_{grav} , Q_{cap} , and Q in ridge 1, and the slopes of the lines of best fit to the numerical results for $T \geq 10^{9/4}$ shown in Fig. 12.

	Asymptotic scaling	Numerical result
H	-0.45	-0.4736
Q_{grav}	-1.35	-1.4179
Q_{cap}	-1.35	-1.3658
Q	-1.50	-1.4828

Since the $O(T^{-3/20}) \ll 1$ width of ridge 1 is asymptotically larger than both the $O(T^{-3/10}) \ll 1$ width of dimple 1 and the width of dimple 2 (which we will shall determine in Sec. VIC), the shape of the interface of ridge 1 is determined by solving Eq. (52) for ϕ_1 subject to appropriate boundary conditions on a finite (rather than an infinite) domain. Specifically, we solve Eq. (52) in the finite domain $\zeta_{1,0} \leq \zeta_1 \leq \zeta_{1,1}$, where the values of $\zeta_{1,0}$ and $\zeta_{1,1}$ are determined as part of the solution, subject to boundary conditions arising from asymptotic matching with dimple 1 at $\zeta_1 = \zeta_{1,1}$, i.e.,

$$\phi_1|_{\zeta_1=\zeta_{1,1}} = 0 \quad \text{and} \quad \phi_{1,\zeta_1}|_{\zeta_1=\zeta_{1,1}} = -m_1, \quad (55)$$

where m_1 is defined by

$$m_1 = K^{1/5} L_0^{1/5} \tilde{m}, \quad (56)$$

and the numerical value of \tilde{m} is given by Eq. (46), and asymptotic matching with dimple 2 at $\zeta_1 = \zeta_{1,0}$, i.e.,

$$\phi_1|_{\zeta_1=\zeta_{1,0}} = 0 \quad \text{and} \quad \phi_{1,\zeta_1}|_{\zeta_1=\zeta_{1,0}} = 0. \quad (57)$$

The final boundary condition fixes the location of the minimum of ϕ_1 at $\zeta_1 = 0$, i.e.,

$$\phi_{1,\zeta_1}|_{\zeta_1=0} = 0. \quad (58)$$

Solving Eq. (52) subject to Eqs. (55)–(58) yields the solution for the interface of ridge 1, namely

$$\phi_1 = \frac{8\sqrt{6}(K^{1/5}L_0^{1/5}\tilde{m})^{3/2} - 9\gamma|\cos\theta_1|\zeta_1^2[\sqrt{6}(K^{1/5}L_0^{1/5}\tilde{m})^{1/2} + (\gamma|\cos\theta_1|)^{1/2}\zeta_1]}{54(\gamma|\cos\theta_1|)^{1/2}}, \quad (59)$$

where $\zeta_{1,0}$ and $\zeta_{1,1}$ are given by

$$\zeta_{1,0} = -\left(\frac{8K^{1/5}L_0^{1/5}\tilde{m}}{3\gamma|\cos\theta_1|}\right)^{1/2} \quad \text{and} \quad \zeta_{1,1} = \left(\frac{2K^{1/5}L_0^{1/5}\tilde{m}}{3\gamma|\cos\theta_1|}\right)^{1/2}, \quad (60)$$

respectively, γ and θ_1 are related by Eq. (25), and L_0 is given by Eq. (37). For example, the solution in ridge 1 for $\gamma = \gamma_\pi$ given by Eq. (8) is

$$\phi_1 = 0.5776 - 2.6949\zeta_1^2 - 2.2405\zeta_1^3. \quad (61)$$

Figure 13 shows snapshots of the film thickness for $\gamma = \gamma_\pi$ given by Eq. (8) at various times together with the leading-order asymptotic solution in ridge 1 (61) expressed in scaled variables ζ_1 and ϕ_1 , confirming that the interface does indeed approach the asymptotic solution at late times. Figure 13 also reveals that the convergence to the leading-order asymptotic solution in ridge 1 is significantly slower than the corresponding convergence in dimple 1 shown in Fig. 11(b): we will return to this point in Sec. VIC.

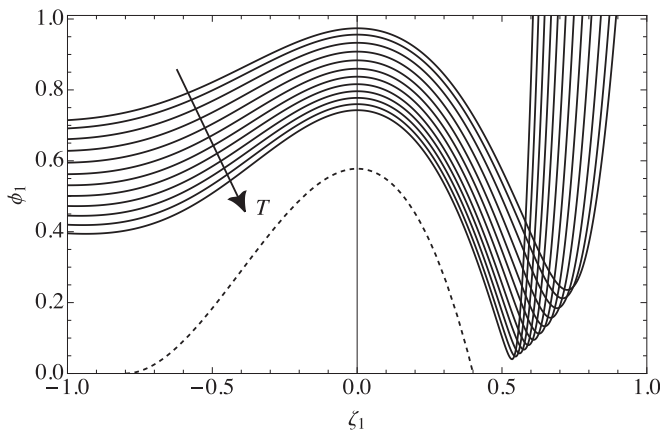


FIG. 13. Snapshots of the film thickness for $\gamma = \gamma_\pi$ given by Eq. (8) at times $T = 10^5 + 10^{n/2}$ for $n = 10, 11, \dots, 21$ expressed in scaled variables ζ_1 and ϕ_1 . The arrow indicates the direction of increasing time. The dashed line shows the leading-order asymptotic solution in ridge 1 (61).

C. Dimple n and ridge n

As discussed previously, the inner region has a capillary-ripple structure consisting of an infinite sequence of dimples and ridges, and Fig. 14 shows sketches of the leading-order asymptotic solutions in dimple n and ridge n for $n = 2, 3, 4, \dots$. Fortunately, the asymptotic solutions for H in all of the dimples and ridges can be obtained by generalizing the analysis for dimple 1 and ridge 1 described in Secs. VIA and VIB, respectively. Specifically, we seek leading-order asymptotic solutions for H in dimple n in the form

$$H = \frac{\psi_n(\xi_n)}{T^{\alpha_n}}, \quad \theta - \theta_1 = \frac{\xi_n}{T^{\beta_n}}, \quad (62)$$

and for H in ridge n in the form

$$H = \frac{\phi_n(\zeta_n)}{T^{\delta_n}}, \quad \theta - \theta_1 = \frac{\zeta_n}{T^{\lambda_n}}, \quad (63)$$

where the exponents $\alpha_n > 1/2$, $\beta_n > 0$, $0 < \delta_n < 1/2$, and $0 < \lambda_n < \min(\beta_n, \beta_{n+1})$ are positive constants.

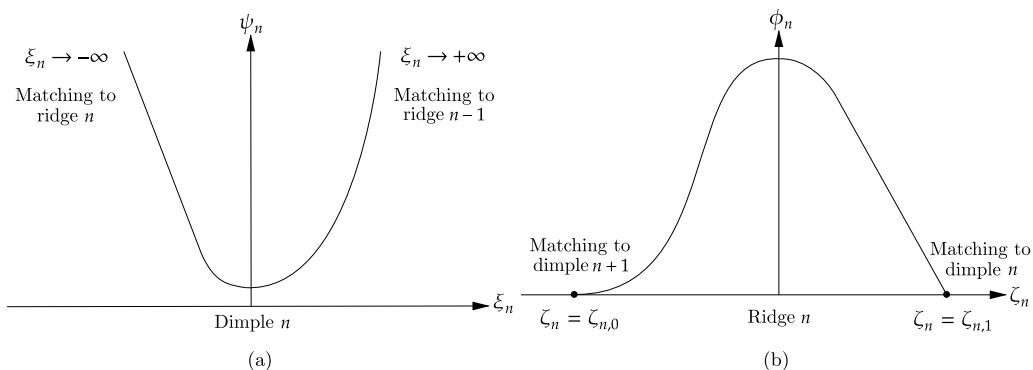


FIG. 14. Sketches of the leading-order asymptotic solutions in (a) dimple n and (b) ridge n for $n = 2, 3, 4, \dots$

Equating the flux from the draining region with the flux in dimple n yields

$$-\frac{3}{2} = -4\alpha_n + 3\beta_n, \quad (64)$$

while matching dimple n with ridge $n - 1$ requires that

$$-\alpha_n + 2\beta_n = -\delta_{n-1} + 2\lambda_{n-1}. \quad (65)$$

On the other hand, equating the flux from the draining region with the flux in ridge n yields

$$\delta_n - 3\lambda_n = 0, \quad (66)$$

while matching ridge n with dimple n requires that

$$-\delta_n + \lambda_n = -\alpha_n + \beta_n. \quad (67)$$

Solving Eqs. (64)–(67) yields

$$\alpha_n = \frac{1}{2}(1 + 2 \times 10^{-n}), \quad \beta_n = \frac{1}{6}(1 + 8 \times 10^{-n}), \quad (68)$$

$$\delta_n = \frac{1}{2}(1 - 10^{-n}), \quad \lambda_n = \frac{1}{6}(1 - 10^{-n}), \quad (69)$$

so that the solution for H in dimple n (62) becomes

$$H = \frac{\psi_n(\xi_n)}{T^{(1+2 \times 10^{-n})/2}}, \quad \theta - \theta_1 = \frac{\xi_n}{T^{(1+8 \times 10^{-n})/6}}, \quad (70)$$

and the solution for H in ridge n (63) becomes

$$H = \frac{\phi_n(\zeta_n)}{T^{(1-10^{-n})/2}}, \quad \theta - \theta_1 = \frac{\zeta_n}{T^{(1-10^{-n})/6}}. \quad (71)$$

Note that setting $n = 1$ in Eqs. (68)–(71) recovers the corresponding results for dimple 1 and ridge 1 obtained in Secs. VI A and VI B, respectively. Furthermore, note that $\alpha_n \rightarrow 1/2^+$ and $\delta_n \rightarrow 1/2^-$ in the limit $n \rightarrow \infty$, confirming that an infinite sequence of dimples and ridges is required to achieve matching with the draining region. Moreover, as n increases these exponents approach to their common asymptotic value rather quickly, explaining why only the first three dimples and ridges are discernible in Fig. 4(b). This is also the reason why the $O(T^{-51/100})/O(T^{-9/20}) = O(T^{-3/50}) \ll 1$ convergence to the leading-order asymptotic solution in ridge 1 shown in Fig. 13 is significantly slower than the corresponding $O(T^{-9/20})/O(T^{-3/5}) = O(T^{-3/20}) \ll 1$ convergence in dimple 1 shown in Fig. 11(b). In addition, note that the values of the exponents given in Eqs. (68) and (69) mean that all of the dimples are narrower than all of the ridges (specifically, the width of dimple n is $O(T^{-\beta_n}) \ll 1$ and the width of ridge n is $O(T^{-\lambda_n}) \ll 1$, where $\beta_n > 1/6$ and $\lambda_n < 1/6$).

Generalizing the approach described in Secs. VI A and VI B shows that in dimple n the function $\psi_n = \psi_n(\xi_n)$ satisfies

$$\psi_n^3 \psi_{n\xi_n\xi_n\xi_n} = K, \quad (72)$$

where K is again given by Eq. (30), subject to

$$\psi_{n\xi_n\xi_n} |_{\xi_n \rightarrow +\infty} = L_{n-1} := \phi_{n-1} |_{\zeta_{n-1} \rightarrow \zeta_{n-1,0}^+}, \quad (73)$$

$$\psi_{n\xi_n\xi_n} |_{\xi_n \rightarrow -\infty} = 0, \quad (74)$$

$$\psi_{n\xi_n} |_{\xi_n=0} = 0, \quad (75)$$

while in ridge n the function $\phi_n = \phi_n(\zeta_n)$ satisfies

$$\phi_{n\zeta_n\zeta_n\zeta_n} = \gamma \cos \theta_1 \quad (76)$$

on the finite domain $\zeta_n \in [\zeta_{n,0}, \zeta_{n,1}]$ subject to

$$\phi_n|_{\zeta_n=\zeta_{n,1}} = 0 \quad \text{and} \quad \phi_{n\zeta_n}|_{\zeta_n=\zeta_{n,1}} = -m_n, \quad (77)$$

$$\phi_n|_{\zeta_n=\zeta_{n,0}} = 0 \quad \text{and} \quad \phi_{n\zeta_n}|_{\zeta_n=\zeta_{n,0}} = 0, \quad (78)$$

$$\phi_{n\zeta_n}|_{\zeta_n=0} = 0. \quad (79)$$

The constants K and L_{n-1} can be scaled out of the problem (72)–(75) by setting

$$\psi_n = K^{2/5} L_{n-1}^{-3/5} \tilde{\psi}, \quad \xi_n = K^{1/5} L_{n-1}^{-4/5} \tilde{\xi}, \quad (80)$$

to exactly recover the rescaled problem (41)–(44) obtained in Sec. VI B, and so m_n is given by

$$m_n = K^{1/5} L_{n-1}^{1/5} \tilde{m}, \quad (81)$$

where the numerical value of \tilde{m} is again given by Eq. (46).

Solving Eq. (76) subject to Eqs. (77)–(79) yields the solution for the interface of ridge n , namely

$$\phi_n = \frac{8\sqrt{6}(K^{1/5} L_{n-1}^{1/5} \tilde{m})^{3/2} - 9\gamma |\cos \theta_1| \zeta_n^2 [\sqrt{6}(K^{1/5} L_{n-1}^{1/5} \tilde{m})^{1/2} + (\gamma |\cos \theta_1|)^{1/2} \zeta_n]}{54(\gamma |\cos \theta_1|)^{1/2}}, \quad (82)$$

where $\zeta_{n,0}$ and $\zeta_{n,1}$ are given by

$$\zeta_{n,0} = -\left(\frac{8K^{1/5} L_{n-1}^{1/5} \tilde{m}}{3\gamma |\cos \theta_1|}\right)^{1/2}, \quad \zeta_{n,1} = \left(\frac{2K^{1/5} L_{n-1}^{1/5} \tilde{m}}{3\gamma |\cos \theta_1|}\right)^{1/2}, \quad (83)$$

respectively, γ and θ_1 are again related by Eq. (25), and L_{n-1} is given by Eq. (73).

Using Eq. (74) we can obtain L_n terms of L_{n-1} , and hence inductively in terms of L_0 . Differentiating Eq. (82) twice with respect to ζ_n and evaluating at $\zeta_n = \zeta_{n,0}$ given by Eq. (83) yields

$$L_n = \sqrt{\frac{2}{3}} (K^{1/5} L_{n-1}^{1/5} \tilde{m} \gamma |\cos \theta_1|)^{1/2}, \quad (84)$$

which can be written in terms of L_0 given by Eq. (37) as

$$L_n = \left(\frac{2}{3} \tilde{m} \gamma |\cos \theta_1|\right)^{x/2} K^y L_0^{10^{-n}}, \quad (85)$$

where the exponents x and y are given by

$$x = \sum_{i=1}^n \frac{1}{10^{i-1}} = \frac{10}{9} (1 - 10^{-n}), \quad y = \sum_{i=1}^n \frac{1}{10^i} = \frac{1}{9} (1 - 10^{-n}), \quad (86)$$

respectively.

The problem for ψ_n (which has to be solved numerically) and the solution for ϕ_n [given by Eqs. (82) and (83)] are now given in terms of known constants, namely K given by Eq. (30), L_0 given by Eq. (37), and \tilde{m} given by Eq. (46), and so the leading-order shape of the interface can now be obtained throughout the inner region.

VII. CONCLUSIONS

In the present work we used a combination of analytical and numerical techniques to give a complete description of the late-time draining of a two-dimensional thin film on the outer surface of a stationary horizontal circular cylinder. In this limit three regions of qualitatively different behavior emerge, namely a draining region on the upper part of the cylinder and a pendant-drop region on the lower part of the cylinder joined by a narrow inner region, as sketched in Fig. 1.

In the draining region, gravity dominates capillarity, the flux decreases as $T^{-3/2} \ll 1$, and the film thins as $T^{-1/2} \ll 1$. The thickness of the film in the draining region is given by Eq. (14), which

shows that at any instant in time the leading-order film thickness in this region increases from a minimum value given by Eq. (15) at the top of the cylinder to a maximum value at $\theta = \theta_1$.

In the pendant-drop region (which, to leading order, contains all of the liquid initially on the cylinder), there is a quasistatic balance between gravity and capillarity. The thickness of the film in the pendant-drop region is given by Eq. (23), which shows that the leading-order film thickness in this region increases from zero at $\theta_1 = \pi$ to a maximum value given by Eq. (26) at the bottom of the cylinder.

The solutions in the draining and pendant-drop regions match via the inner region located at $\theta = \theta_1$, where θ_1 is given implicitly by Eq. (25). In particular, Eq. (25) shows that weakening the effect of gravity results in a narrower draining region and a wider pendant-drop region. Within the inner region the film has a capillary-ripple structure consisting of an infinite sequence of alternating dimples and ridges, as sketched in Fig. 14. Gravity is negligible in the dimples, which are all thinner than the film in the draining region (specifically, the thickness of dimple n is $O(T^{-\alpha_n}) \ll 1$, where $\alpha_n > 1/2$). On the other hand, gravity and capillarity are comparable in the ridges, which are all thicker than the film in the draining region (specifically, the thickness of ridge n is $O(T^{-\delta_n}) \ll 1$, where $\delta_n < 1/2$). The dimples and the ridges are all asymmetric: specifically, the leading-order thickness of the dimples grows quadratically in the downstream direction but linearly in the upstream direction, whereas the leading-order thickness of the ridges goes to zero linearly in the downstream direction but quadratically in the upstream direction. Matching between the inner and the draining region is achieved in the limit $n \rightarrow \infty$, in which the exponents α_n and δ_n both approach their common asymptotic value of $1/2$. The asymptotic solutions in the draining and pendant-drop regions, as well as those in dimple 1 and ridge 1 in the inner region, were verified by comparison with numerical solutions of the governing thin-film equation. As Fig. 6 illustrates, as T increases the regions that have the largest deviation from the $O(T^{-1/2})$ thickness of the draining region (namely, dimple 1 followed by ridge 1) are the first to become discernible, with the other dimples and ridges subsequently becoming apparent in turn. However, since the exponents α_n and δ_n both approach $1/2$ rather quickly as n increases [specifically, α_n and β_n both only differ from $1/2$ by $O(10^{-n})$], the other dimples and ridges only become apparent for rather large values of T , i.e., only the first few dimples and ridges are likely to be discernible for large but finite times. This is presumably the reason why the corresponding infinite sequence of dimples and ridges was overlooked by Qin *et al.* [15] in their study of the corresponding problem on a spherical substrate.

While several aspects of the structure of the late-time solution described in the present work have been described by previous authors, such as the formation of a pendant drop on the lower part of the cylinder discussed by Reisfeld and Bankoff [11] and Evans *et al.* [12] and the thinning of the film on the upper part of the cylinder analyzed by Takagi and Huppert [13], the present work is the first to provide a complete description of it. In particular, the present work is the first to describe the surprisingly complicated capillary-ripple structure of the inner region which joins the draining and pendant-drop regions.

Note that the late times for which the present analysis is relevant may, in practice, correspond to only minutes or hours. For example, using the representative dimensional parameter values $\hat{R} = 0.1$ m, $\hat{\rho} = 10^3$ kg m³, and $\hat{\mu} = 10^{-3}$ kg m⁻¹ s⁻¹, together with $\epsilon = 0.1$, yields a characteristic timescale of $\hat{R}/(\epsilon^2 \hat{U}_{\text{ref}}) = \hat{\mu}/(\epsilon^2 \hat{\rho} \hat{g} \hat{R}) = O(10^{-4})$ s. Hence, $T = O(10^6)$, for which the present late-time asymptotic solution already provides a good description of the flow, corresponds to about 2 minutes. Of course, as the film thins disjoining pressure effects, which are not included in the present analysis, will eventually become important. Specifically, for the representative parameter values used previously together with $\hat{\sigma} = 10^{-1}$ N m⁻¹ and Hamaker constant $\hat{A} = 10^{-20}$ J, disjoining pressure due to van der Waals forces (see, for example, Reisfeld and Bankoff [11]) becomes comparable to the pressure due to capillarity in dimple 1 [where the film is thinnest and $H = O(T^{-3/5})$] when $T = O(10^8)$, corresponding to about 3 hours. Hence, while the longest final times of up to $T = O(10^{11})$ required to validate the present asymptotic solution correspond to around four months and are therefore almost certainly unphysical, there is likely to be a considerable period of time during which the present asymptotic solution provides a good description of the flow.

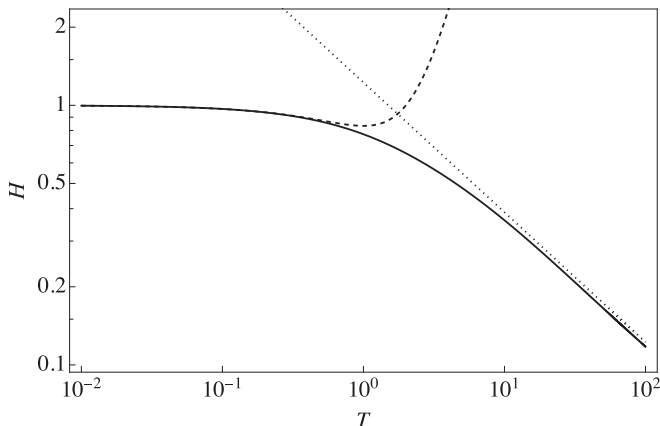


FIG. 15. The evolution of the film thickness at the top of the cylinder for $\gamma = \gamma_\pi$ given by Eq. (8) until time $T = 10^2$. The solid line shows the numerical solution of Eq. (4), the dashed line shows the early-time asymptotic solution (A1), and the dotted line shows the late-time asymptotic solution (15).

Finally, we note that all of the results in the present work were based on the assumption that the film is thin and is therefore governed by the thin-film equation (4) with Q given by Eq. (5), and so it would be of interest to see to what extent these results still hold for nonthin films governed by the full Navier–Stokes equation.

ACKNOWLEDGMENT

The first author (R.McK.) gratefully acknowledges the support of the Carnegie Trust for the Universities of Scotland via a PhD Scholarship.

APPENDIX: EARLY-TIME DRAINING

In this Appendix, we briefly describe the draining of the initially uniform film at early times. As in the corresponding problem of flow on a spherical substrate studied by Qin *et al.* [15], the asymptotic solution for the film thickness $H = H(\theta, T)$ at early times is found by expanding it in powers of $T \ll 1$ and solving order by order to obtain

$$H = 1 - \frac{T}{3} \sin \theta - \frac{T^2}{6} \cos(2\theta) + O(T^3). \quad (\text{A1})$$

The absence of γ from Eq. (A1) shows that, as expected given its small deviation from uniformity, at early times the evolution of the film is independent of capillarity up to at least $O(T^2) \ll 1$. Figure 15 shows the evolution of the film thickness at the top of the cylinder for $\gamma = \gamma_\pi$ given by Eq. (8) until time $T = 10^2$, and confirms that the early-time asymptotic solution (A1) (shown with the dashed line) is valid at the top of the cylinder at early times. For completeness, Fig. 15 also includes the corresponding late-time asymptotic solution (15) (shown with the dotted line) and confirms that it is valid at late times.

[1] S. F. Kistler and P. M. Schweizer, *Liquid Film Coating* (Springer, Dordrecht, 1997).

[2] N. K. Akafuah, S. Poozesh, A. Salaimeh, G. Patrick, K. Lawler, and K. Saito, Evolution of the automotive body coating process—A review, *Coatings* **6**, 24 (2016).

-
- [3] G. Ribatski and A. M. Jacobi, Falling-film evaporation on horizontal tubes—A critical review, *Int. J. Refrig.* **28**, 635 (2005).
- [4] B. W. Minifie, *Chocolate, Cocoa and Confectionery: Science and Technology*, 3rd ed. (Chapman & Hall, Oxford, UK, 1989).
- [5] B. G. X. Zhang, D. E. Myers, G. G. Wallace, M. Brandt, and P. F. M. Choong, Bioactive coatings for orthopaedic implants—Recent trends in development of implant coatings, *Int. J. Mol. Sci.* **15**, 11878 (2014).
- [6] R. J. Braun, R. Usha, G. B. McFadden, T. A. Driscoll, L. P. Cook, and P. E. King-Smith, Thin film dynamics on a prolate spheroid with application to the cornea, *J. Eng. Math.* **73**, 121 (2012).
- [7] J. B. Grotberg, Pulmonary flow and transport phenomena, *Annu. Rev. Fluid Mech.* **26**, 529 (1994).
- [8] W. Nusselt, Die oberflächenkondensation des wasserdampfes, *Z. Vereines deutscher Ingenieure* **60**, 541 (1916).
- [9] W. Nusselt, Die oberflächenkondensation des wasserdampfes, *Z. Vereines deutscher Ingenieure* **60**, 569 (1916).
- [10] B. R. Duffy and S. K. Wilson, Thin-film and curtain flows on the outside of a rotating horizontal cylinder, *J. Fluid Mech.* **394**, 29 (1999).
- [11] B. Reisfeld and S. G. Bankoff, Non-isothermal flow of a liquid film on a horizontal cylinder, *J. Fluid Mech.* **236**, 167 (1992).
- [12] P. L. Evans, L. W. Schwartz, and R. V. Roy, Steady and unsteady solutions for coating flow on a rotating horizontal cylinder: Two-dimensional theoretical and numerical modeling, *Phys. Fluids* **16**, 2742 (2004).
- [13] D. Takagi and H. E. Huppert, Flow and instability of thin films on a cylinder and sphere, *J. Fluid Mech.* **647**, 221 (2010).
- [14] M. Cachile, M. A. Aguirre, M. Lenschen, and A. Calvo, Flow of a thin liquid film coating a horizontal stationary cylinder, *Phys. Rev. E* **88**, 063005 (2013).
- [15] J. Qin, Y. Xia, and P. Gao, Axisymmetric evolution of gravity-driven thin films on a small sphere, *J. Fluid Mech.* **907**, A4 (2021).
- [16] D. Kang, A. Nadim, and M. Chugnova, Marangoni effects on a thin liquid film coating a sphere with axial or radial thermal gradients, *Phys. Fluids* **29**, 072106 (2017).
- [17] H. González, F. M. J. McCluskey, A. Castellanos, and A. Barrero, Stabilization of dielectric liquid bridges by electric fields in the absence of gravity, *J. Fluid Mech.* **206**, 545 (1989).
- [18] A. Oron, S. H. Davis, and S. G. Bankoff, Long-scale evolution of thin liquid films, *Rev. Mod. Phys.* **69**, 931 (1997).
- [19] R. V. Craster and O. K. Matar, Dynamics and stability of thin liquid films, *Rev. Mod. Phys.* **81**, 1131 (2009).
- [20] A. W. Wray, D. T. Papageorgiou, and O. K. Matar, Reduced models for thick liquid layers with inertia on highly curved substrates, *SIAM J. Appl. Math.* **77**, 881 (2017).
- [21] A. W. Wray and R. Cimpeanu, Reduced-order modelling of thick inertial flows around rotating cylinders, *J. Fluid Mech.* **898**, A1 (2020).
- [22] Eigen v3, eigen.tuxfamily.org (2010).
- [23] S. D. R. Wilson and A. F. Jones, The entry of a falling film into a pool and the air-entrainment problem, *J. Fluid Mech.* **128**, 219 (1983).
- [24] J. Ashmore, A. E. Hosoi, and H. A. Stone, The effect of surface tension on rimming flows in a partially filled rotating cylinder, *J. Fluid Mech.* **479**, 65 (2003).
- [25] L. Duchemin, J. R. Lister, and U. Lange, Static shapes of levitated viscous drops, *J. Fluid Mech.* **533**, 161 (2005).
- [26] E. S. Benilov, M. S. Benilov, and N. Kopteva, Steady rimming flows with surface tension, *J. Fluid Mech.* **597**, 91 (2008).
- [27] E. S. Benilov, S. J. Chapman, J. B. McLeod, J. R. Ockendon, and V. S. Zubkov, On liquid films on an inclined plate, *J. Fluid Mech.* **663**, 53 (2010).
- [28] E. S. Benilov and M. S. Benilov, A thin drop sliding down an inclined plane, *J. Fluid Mech.* **773**, 75 (2015).

- [29] I. J. Hewitt, N. J. Balmforth, and J. R. De Bruyn, Elastic-plated gravity currents, [Eur. J. Appl. Math.](#) **26**, 1 (2015).
- [30] R. Brandão and O. Schnitzer, Leidenfrost levitation of a spherical particle above a liquid bath: Evolution of the vapour-film morphology with particle size, [Eur. J. Appl. Math.](#) **33**, 1117 (2022).
- [31] C. Lamstaes and J. Eggers, Arrested bubble rise in a narrow tube, [J. Stat. Phys.](#) **167**, 656 (2017).
- [32] M. A. J. van Limbeek, B. Sobac, A. Rednikov, P. Colinet, and J. H. Snoeijer, Asymptotic theory for a Leidenfrost drop on a liquid pool, [J. Fluid Mech.](#) **863**, 1157 (2019).